Supplementary Information: Quantification of magnetization of nanostructures via three complementary methods

Xianhui Ye,[1] Hangbo Su,[1] Jiaqi Su,[1] András Kovács,[2] Marco Beleggia,[3] Rafal E. Dunin-Borkowski,[2] and Zi-An Li[1, a)]

[1)] *School of Physical Science and Technology, and State Key Laboratory of Featured Metal Materials and Life-cycle Safety for Composite Structures, Guangxi University, Nanning 530004, China*

[2)] *Ernst Ruska-Centre for Microscopy and Spectroscopy with Electrons (ER-C 1) and Peter Grünberg Institute (PGI 5), Forschungszentrum Jülich GmbH, 52425 Jülich, Germany*

[3)] *Department of Physics, University of Modena and Reggio Emilia, 41125 Modena, Italy*

(Dated: 27 May 2025)

S1: REPRESENTATIVE OFF-AXIS ELECTRON HOLOGRAM

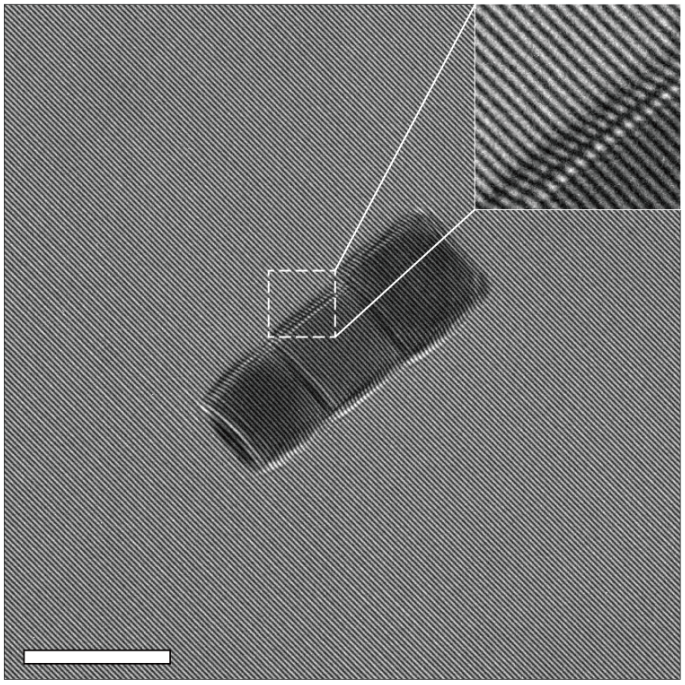

FIG. S1. Off-axis electron hologram of Fe_3O_4 particles, showing well-resolved holographic interference fringes with a spacing of approximately 2.7 nm. The scale bar represents 100 nm. The inset shows magnified holographic interference fringes around the middle particle.

S2: REPRESENTATIVE PHASE IMAGES

Figure S2(a) shows the magnetic vector potential contribution to the phase of the Fe_3O_4 particles and a corresponding phase contour map. The asymmetry of the phase contours may stem from magnetization sources located

[a)] Corresponding author: zianli@gxu.edu.cn

outside the field of view or from artifacts such as specimen charging or changes to the biprism wire over time. Figure S2(b) shows the ramp-corrected phase image, obtained by subtracting the fitted ramp shown in Figure S2(d).

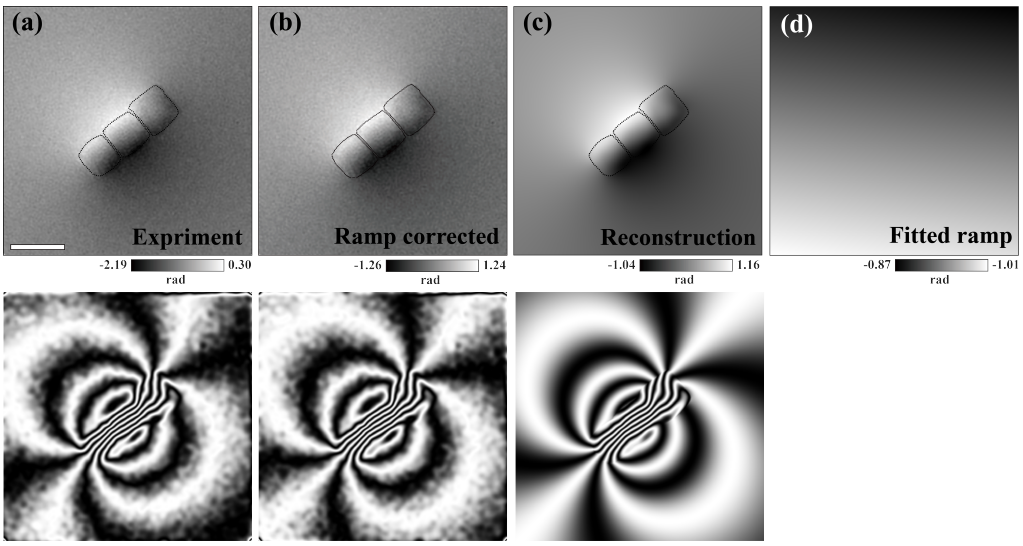

FIG. S2. Phase images (top) and corresponding phase contour maps (bottom). The scale bar represents 100 nm. (a) Magnetic vector potential contribution to the phase measured from Fe_3O_4 particles. (b) Ramp correction applied to (a). (c) Magnetic phase image calculated by applying the forward model to the reconstructed magnetisation distribution shown in Figure 5a (left). (d) Reconstruction of the additional phase ramp.

S3: PHASE INTEGRAL

To clarify the derivation of the inductive moment $\boldsymbol{m}_B$, we begin with the standard definition of the inductive moment as the volume integral of the magnetic induction $\boldsymbol{B}$:

$$\boldsymbol{m}_B = \frac{1}{\mu_0} \iiint_V \boldsymbol{B}(\boldsymbol{r})\, d^3\boldsymbol{r}$$

Since the magnetic induction $\boldsymbol{B}$ is related to the magnetic vector potential $\boldsymbol{A}$ through $\boldsymbol{B} = \nabla \times \boldsymbol{A}$, we can rewrite the above expression using vector calculus identities. Applying Gauss's theorem to the curl of $\boldsymbol{A}$, and recognizing that the phase shift $\varphi(\boldsymbol{r})$ obtained from off-axis electron holography is proportional to the line integral of the in-plane magnetic vector potential, we arrive at a relationship between the inductive moment and a contour integral of the phase shift:

$$\boldsymbol{m}_B \propto \oint_{\partial S} \varphi(\boldsymbol{r})\, \hat{t}(\theta)\, d\theta$$

In this expression, the integral is taken over a circular path with radius R, and $\hat{t}(\theta)$ represents the unit tangential vector along the path. The direction of the tangential vector $\hat{t}(\theta) = [-\sin\theta, \cos\theta]$ follows from differentiating the position vector in polar coordinates $[\cos\theta, \sin\theta]$, defining the direction along which the phase gradient is projected.

This leads to the following expression for the inductive moment[1]:

$$\boldsymbol{m}_B = \frac{\hbar R}{e\mu_0} \int_0^{2\pi} \varphi(R\cos\theta, R\sin\theta) \begin{bmatrix} -\sin\theta \\ \cos\theta \end{bmatrix} d\theta$$

The vector integral can then be separated into its x- and y-components:

$$m_{Bx} = \frac{\hbar R}{e\mu_0} \int_0^{2\pi} -\varphi(R\cos\theta, R\sin\theta)\sin\theta\, d\theta$$

$$m_{By} = \frac{\hbar R}{e\mu_0} \int_0^{2\pi} \varphi(R\cos\theta, R\sin\theta)\cos\theta\, d\theta$$

Through this decomposition, the vector inductive moment $\boldsymbol{m}_B = (m_{Bx}, m_{By})$ is reconstructed, and its orientation in the plane can be determined by:

$$\theta_m = \arctan\left(\frac{m_{By}}{m_{Bx}}\right)$$

S4: MEASUREMENT ERRORS ASSESSMENT

The calculated phase image shown in Figure S2(c) can be used to retrospectively assess the measurement errors in the input phase image shown in Figure S2(a). To do this, the input phase image was first ramp-corrected by subtracting the fitted phase ramp. The difference between the ramp-corrected input phase and the phase calculated from the reconstructed magnetization is shown in Figure S3(a). By plotting the resulting phase differences in a histogram, as shown in Figure S3(b), a Gaussian distribution is revealed, with a standard deviation of 45.16 mrad, which provides an estimate of the measurement noise.

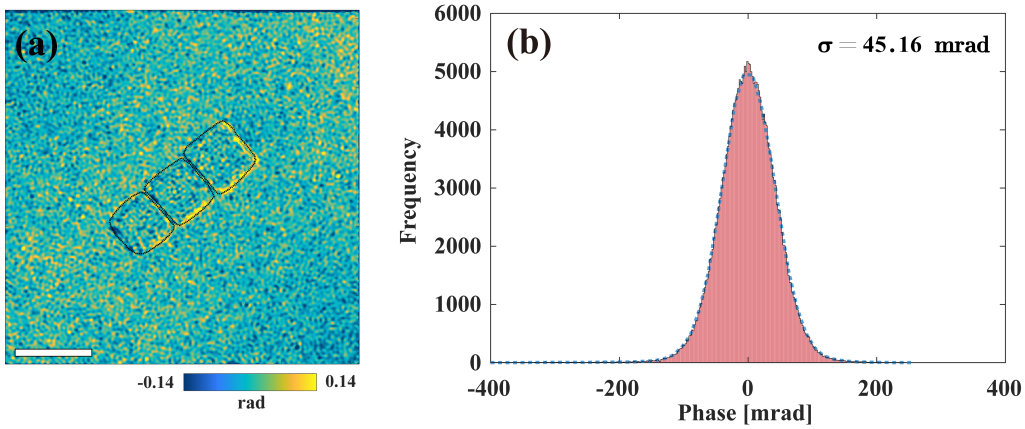

FIG. S3. (a) Difference between the experimental magnetic phase image and the phase image calculated from the reconstructed magnetisation distribution. The scale bar represents 100 nm. (b) Histogram of the phase differences. The standard deviation of 45.16 mrad is an indicator for the measurement error of the phase image.

S5: SAMPLE THICKNESS ESTIMATION

Sample thickness was estimated by measuring the phase shift caused by the MIP and using the known accelerating voltage and the MIP value for magnetite. According to the electrostatic phase shift equation: $\varphi_E = C_E \cdot V_0 \cdot t$, where φ_E is the electrostatic phase shift, V_0 is the assumed MIP of magnetite[2], approximately 17 V, C_E is the electron interaction constant, which has a value of 6.53×10^6 rad V^{-1} m^{-1}, and t is the sample thickness. By measuring the electrostatic phase distribution along the long edge of the selected particle in Figure S4(a), we estimate the nanoparticle thickness. For a cubic magnetite nanoparticle with a side length of 73 nm, the predicted MIP-induced phase shift at the center is 8.10 rad, closely matching the measured value of 8.11 rad. Hence, the nanoparticle thickness is estimated to be 73 nm.

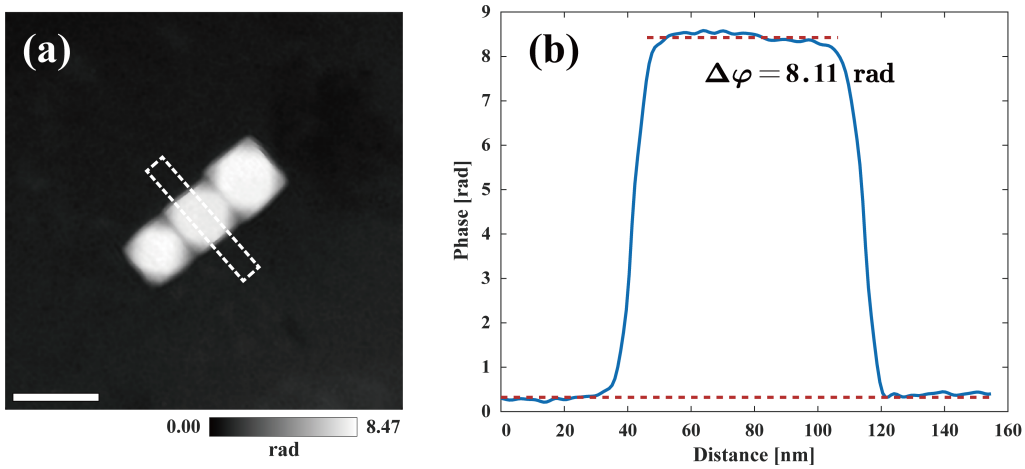

FIG. S4. (a) MIP contribution to the phase measured from Fe_3O_4 particles. The scale bar represents 100 nm. (b) Phase profile of the white box from left to right along the long side (a).

S6: NONLINEAR LEAST-SQUARES FITTING

Sphere Fit

To analyze the phase distribution obtained through electron holography, a nonlinear least-squares fitting approach was employed to extract the perpendicular magnetic field component ($B_\perp$) from the phase map. The fitting model is based on the theoretical relationship between the electron-optical phase and the magnetic field distribution, with the nanoparticle assumed to be spherical. The model for the magnetic field is expressed as[3]:

$$f(B_\perp, x) = \begin{cases} \frac{e}{\hbar} B_\perp \frac{a^3 - \left(a^2 - x^2\right)^{3/2}}{x+\epsilon}, & |x| \le a, \\ \frac{e}{\hbar} B_\perp \frac{a^3}{x+\epsilon}, & |x| > a, \end{cases}$$

where a is the radius of the uniformly magnetized nanoparticle, and ϵ is a small positive constant (10^{-10}) introduced to avoid division by zero at $x = 0$. The fitting procedure began with an initial guess for $B_\perp = 0.6$ T, which corresponds to the saturation magnetization of the nanoparticle. The optimization aimed to minimize the residual sum of squares between the experimental data and the theoretical model.

To evaluate the robustness of the fitting results, the covariance matrix was computed from the Jacobian matrix obtained during the fitting process. The covariance matrix is given by:

$$\text{Cov} = \frac{\text{Resnorm}}{N - P} \left(J^T J\right)^{-1},$$

where N is the number of data points, P is the number of fitting parameters, and J is the Jacobian matrix. The diagonal elements of the covariance matrix provide the standard errors for $B_\perp$.

Additionally, we assessed the impact of uncertainties in the characteristic radius a on the fitted $B_\perp$ values by performing the fitting process with perturbed values of a, specifically $a + \Delta a$ and $a - \Delta a$, where Δa represents a 5% relative uncertainty in a. The sensitivity of $B_\perp$ to changes in a was evaluated using numerical differentiation:

$$\frac{\partial B_\perp}{\partial a} = \frac{B_\perp(a + \Delta a) - B_\perp(a - \Delta a)}{2\Delta a}.$$

This sensitivity analysis allows us to estimate the contribution of the uncertainty in a to the total error in $B_\perp$. By combining this with the standard error derived from the covariance matrix, we obtained the final uncertainty for $B_\perp$.

Cube Fit

A similar nonlinear least-squares fitting approach was applied to extract the magnetic field component $B_\perp$ from experimental data, we consider the nanoparticle as a uniformly magnetized cube. Let the cube have length L and the magnetization direction β. The magnetization is given by

$$M = M_0(\cos\beta, \sin\beta, 0).$$

The least-squares fitting model for the magnetic field is expressed as[4]:

$$\begin{aligned}\varphi_m(x,y) = -\frac{\mu_0 M_0 L_z}{4\phi_0}\cos\beta[&F_0(x - \frac{L_x}{2}, y - \frac{L_y}{2}) - F_0(x + \frac{L_x}{2}, y - \frac{L_y}{2}) - \\ &F_0(x - \frac{L_x}{2}, y + \frac{L_y}{2}) + F_0(x + \frac{L_x}{2}, y + \frac{L_y}{2})] + \\ \frac{\mu_0 M_0 L_z}{4\phi_0}\sin\beta[&F_0(y - \frac{L_y}{2}, x - \frac{L_x}{2}) - F_0(y + \frac{L_y}{2}, x - \frac{L_x}{2}) - \\ &F_0(y - \frac{L_y}{2}, x + \frac{L_x}{2}) + F_0(y + \frac{L_y}{2}, x + \frac{L_x}{2})],\end{aligned}$$

where ϕ_0 is the magnetic flux quantum and $F_0(x, y)$ is an identity given by the following expression:

$$F_0(x,y) = \int \log(x^2 + y^2)\mathrm{d}x = x\log(x^2 + y^2) - 2x + 2y\arctan(\frac{x}{y}).$$

The fitting procedure was initiated with an initial guess for $B_\perp = 0.6$ T, which corresponds to the nanoparticle's saturation magnetization. For a line profile taken through the center of the particle in a direction perpendicular to $B_\perp$, the expression simplifies to:

$$\begin{aligned}\varphi_m(x,y)|_{y=0} = -\frac{B_\perp L_z}{4\phi_0}\cos\beta[&F_0(x - \frac{L_x}{2}, -\frac{L_y}{2}) - F_0(x + \frac{L_x}{2}, -\frac{L_y}{2}) - \\ &F_0(x - \frac{L_x}{2}, \frac{L_y}{2}) + F_0(x + \frac{L_x}{2}, \frac{L_y}{2})] + \\ \frac{B_\perp L_z}{4\phi_0}\sin\beta[&F_0(-\frac{L_y}{2}, x - \frac{L_x}{2}) - F_0(\frac{L_y}{2}, x - \frac{L_x}{2}) - \\ &F_0(-\frac{L_y}{2}, x + \frac{L_x}{2}) + F_0(\frac{L_y}{2}, x + \frac{L_x}{2})].\end{aligned}$$

Similarly, we evaluated the impact of uncertainties in the characteristic length L on the fitted $B_\perp$ values by performing the fitting process with perturbed values of L, specifically $L + \Delta L$ and $L - \Delta L$, where ΔL represents a 5% relative uncertainty in L. The sensitivity of $B_\perp$ to changes in L was determined using numerical differentiation:

$$\frac{\partial B_\perp}{\partial L} = \frac{B_\perp(L + \Delta L) - B_\perp(L - \Delta L)}{2\Delta L}.$$

This sensitivity analysis allows us to estimate the contribution of the uncertainty in L to the total error in $B_\perp$. By combining this contribution with the standard error derived from the covariance matrix, we obtained the final uncertainty for $B_\perp$.

S7: MODEL-BASED ITERATIVE MAGNETIZATION RECONSTRUCTION

A model-based approach was employed to reconstruct the projected in-plane magnetization distribution from magnetic phase images obtained via off-axis electron holography. Figure S5(a) illustrates both the forward model and the inverse problem associated with magnetization reconstruction from experimentally acquired magnetic phase images. In this approach, a mask is first applied to delineate the specimen's edge, and an initial estimate for the magnetization distribution $\boldsymbol{M}(x, y)$ is made on a two-dimensional Cartesian grid. A simulated magnetic phase image $\varphi(x, y)$ is then computed from this initial magnetization distribution. To ensure accuracy, known analytical solutions for phase shifts of simple geometric objects are utilized, with numerical discretization carried out in real space to avoid artifacts that may arise from discretization in Fourier space. This forward simulation is incorporated into an iterative scheme to solve the inverse problem, reconstructing the projected in-plane magnetization distribution from a two-dimensional phase image, as depicted in Figure S5(b). The iterative nature of this method allows the integration of additional physical constraints, such as the limitation that the angle between the magnetic moments of adjacent discretized cells cannot exceed a certain threshold. It is crucial to ensure that the size of the discretized cells is smaller than the exchange length of the magnetic material to maintain the accuracy of the reconstruction.

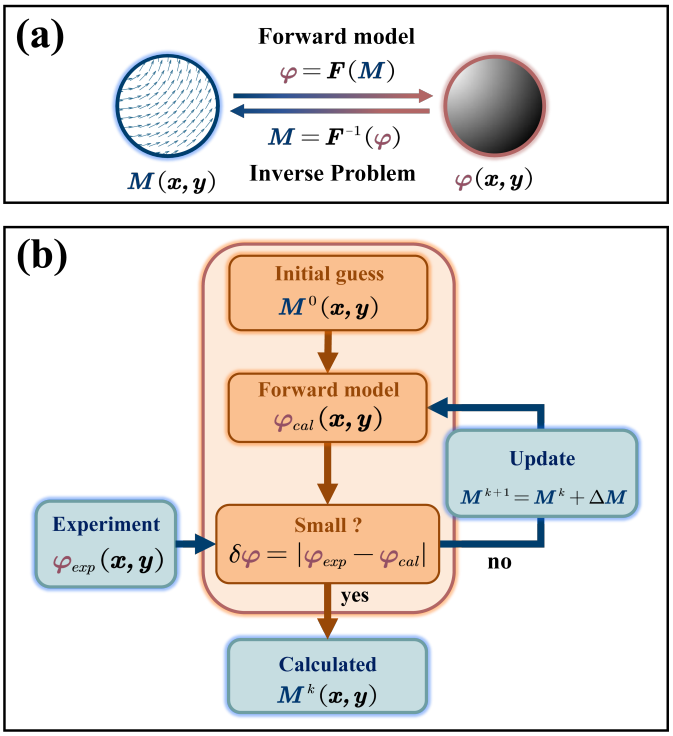

FIG. S5. Schematic of the model-based iterative magnetization reconstruction algorithm used in this study. (a) The forward model and inverse problem. (b) Flowchart illustrating the iterative process for reconstructing the projected in-plane magnetization from an experimental magnetic phase image.

S8: MICROMAGNETIC SIMULATION

Based on two-dimensional transmission electron microscopy (TEM) images, the three-dimensional morphology of the sample was inferred, and truncated cube geometries were constructed to model the Fe_3O_4 nanoparticles[5,6]. To ensure computational accuracy, a cubic mesh size of 3 nm was adopted for discretization, which is smaller than the exchange length of Fe_3O_4 (9.45 nm). Convergence of the simulation results was validated through comparison with a finer 2 nm mesh. The material parameters were set according to the bulk properties of Fe_3O_4[7,8]: saturation magnetization $M_s = 4.85 \times 10^5$ A/m, exchange stiffness $A = 1.32 \times 10^{-11}$ J/m, and first-order cubic magnetocrystalline anisotropy constant $K_1 = -1.36 \times 10^4$ J/m^3, with easy axes along the [111] directions. The Landau–Lifshitz–Gilbert equation was employed to simulate the magnetization dynamics, with the Gilbert damping constant set to $\alpha = 0.5$ to facilitate effective relaxation.

To accurately replicate the experimental magnetization process, the simulation was carried out in two steps: (1) an external magnetic field, equivalent to the objective lens field, was applied to saturate the system; (2) the field was then quasi-statically removed to achieve the remanent state. The simulated magnetization vector field was subsequently projected and integrated along the electron beam direction (z-axis), and the corresponding magnetic phase shift was calculated. In addition, in situ tilting experiments reveal that the upper-right particle develops a clearly observable closed-flux domain structure upon tilting (Figure S6(e)–(h)), consistent with the simulated vortex configuration.

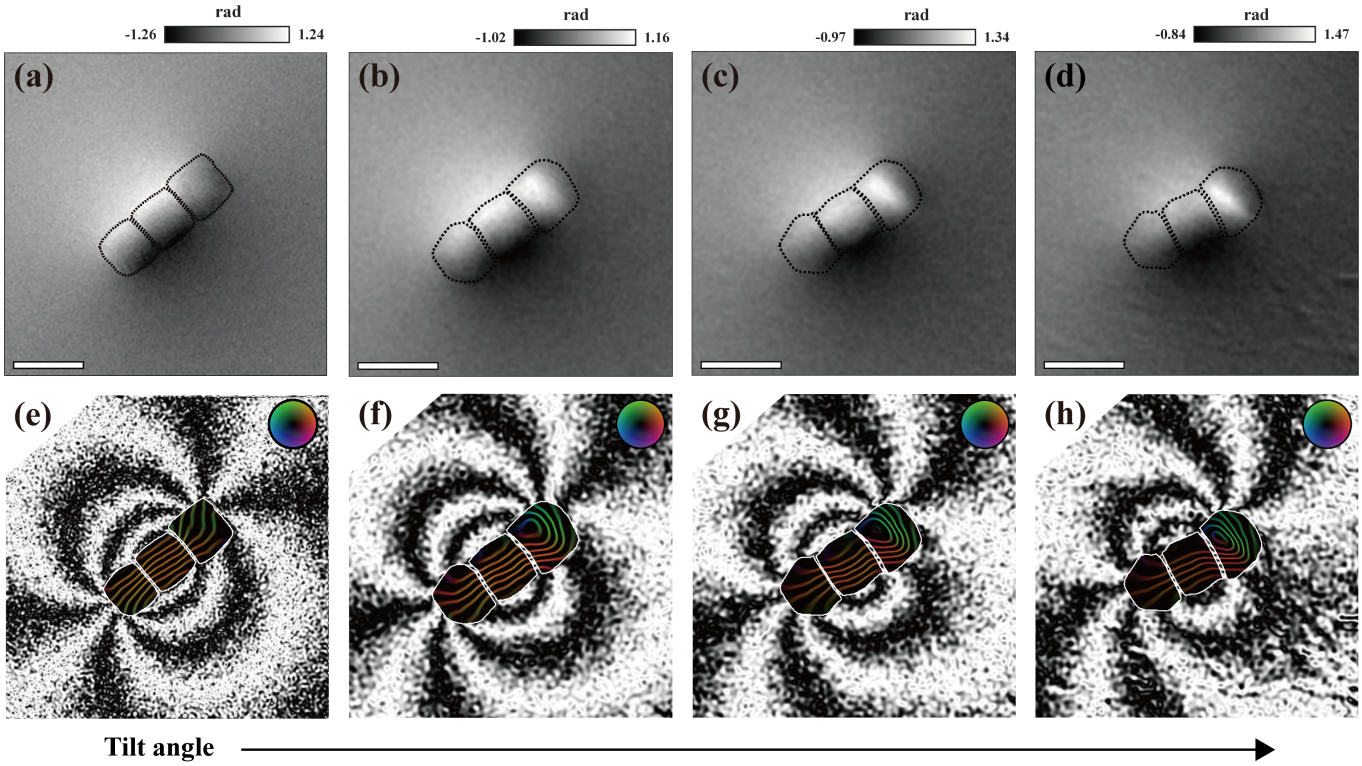

FIG. S6. (a–d) Experimentally obtained magnetic phase shift images with increasing sample tilt angles from left to right. (e–g) Cosine of the experimental phase images, representing the projected magnetic induction flux lines. The induction direction follows the color wheel shown in the inset.

[1]M. Beleggia, T. Kasama, and R. E. Dunin-Borkowski, Ultramicroscopy **110**, 425 (2010).
[2]R. J. Harrison, R. E. Dunin-Borkowski, and A. Putnis, Proceedings of the National Academy of Sciences **99**, 16556 (2002).
[3]M. De Graef, N. Nuhfer, and M. McCartney, Journal of Microscopy **194**, 84 (1999).
[4]K. Keimpema, H. De Raedt, and J. T. M. De Hosson, Journal of Computational and Theoretical Nanoscience **3**, 362 (2006).
[5]D. Kim, N. Lee, M. Park, B. H. Kim, K. An, and T. Hyeon, Journal of the American Chemical Society **131**, 454 (2009).
[6]Y. Takeno, Y. Murakami, T. Sato, T. Tanigaki, H. S. Park, D. Shindo, R. M. Ferguson, and K. M. Krishnan, Applied Physics Letters **105** (2014).
[7]W. Williams, A. R. Muxworthy, and G. A. Paterson, Journal of Geophysical Research: Solid Earth **111** (2006).
[8]A. R. Muxworthy and W. Williams, Journal of Geophysical Research: Solid Earth **111** (2006).